Journal of Materials Chemistry C

ROYAL SOCIETY OF CHEMISTRY

PAPER

View Article Online
View Journal

Cite this: DOI: 10.1039/d6tc00385k

Defect-tuned conduction in ultrathin $MoTe_2$ field-effect transistors

Adolfo Mazzotti,[a] Kimberly Intonti,[a] Andrea Sessa,[a] Loredana Viscardi,[b] Ofelia Durante,[a] Aniello Pelella,[a] Stephen O'Sullivan,[b] Vilas Patil,[b] Paul K. Hurley,[bc] Lida Ansari,[b] Farzan Gity[b] and Antonio Di Bartolomeo *[a]

In atomically thin electronics, interfaces and interfacial defects play a critical role in determining device performance. Herein, interfaces with metal contacts, gate dielectrics, and ambient environments are systematically investigated in p-type field-effect transistors with an ultrathin $MoTe_2$ channel, through temperature- and pressure-dependent measurements, supported by density functional theory calculations. The device performance, likely influenced by Te and Mo vacancies, is enhanced under reduced pressure. Low and nearly symmetric Schottky barrier heights around 37 ± 3 meV are extracted at the metal/semiconductor interfaces through temperature-dependent measurements. The temperature dependence of the mobility suggests that ionized-impurity scattering is possibly associated with Te and Mo vacancies, as a relevant transport mechanism below 300 K, while acoustic-phonon scattering prevails at higher temperatures. Both the subthreshold swing and threshold voltage increase exponentially with temperature, consistent with thermally activated transport mechanisms from band-tail states. A stepwise increase in pressure, starting from vacuum and gradually introducing ambient air, leads to reduced mobility and conductance, which is consistent with progressive molecular physisorption that introduces additional scattering. Near atmospheric pressure, adsorbates are likely to contribute significantly to p-type doping. Taken together, these results elucidate how vacancies, interface traps, and surface adsorbates may govern charge transport in $MoTe_2$ and provide quantitative guidelines for defect and interface engineering that may also be relevant to other two-dimensional semiconductor devices.

Received 5th February 2026,
Accepted 9th April 2026

DOI: 10.1039/d6tc00385k

rsc.li/materials-c

1. Introduction

Two-dimensional materials have attracted increasing attention in recent years since they exhibit properties that are not accessible in conventional three-dimensional crystals.[1–3] As traditional semiconductors approach their scaling limits, low-dimensional semiconductors offer one of the most promising routes to further downscale electronic devices. Significant progress has been made along this direction, and many two-dimensional semiconductors, such as transition metal dichalcogenides (TMDs), have been integrated into high-performance field-effect transistors (FETs).[4–9] They have been widely employed in the development of logic circuits for digital electronics, providing a viable alternative to standard CMOS technology.[10–14] Beyond digital logic, 2D materials have enabled a broad range of device concepts, including photodetectors,[15–17] gas sensors,[18,19] and neuromorphic devices.[20–24] More advanced fabrication and integration strategies have further enabled multifunctional devices based on 2D layered materials, combining memory and computing capabilities and supporting functions such as logic-gate operations, edge-oriented computing, and brain-inspired behaviors including adaptive learning.[25]

Practical device performance is tightly linked to how the 2D material is produced and integrated: scalable growth routes often yield polycrystalline films where grain boundaries and related defects can dominate carrier scattering and recombination, whereas alternative processing routes emphasize interface cleanliness and film quality for robust operation.[26] A central challenge across 2D electronics is therefore stability and defect control. In TMDCs, point defects, impurities, dislocations, and grain boundaries can introduce mid-gap states that act as trap/detrap and recombination centers, affecting mobility, subthreshold swing, hysteresis, and time-dependent responses.[27,28]

Molybdenum ditelluride ($MoTe_2$) is a compound in the TMD family and can be found in both a semiconducting (2H) phase, or in a semi-metallic (1T′) phase with a slight band overlap

[a] Department of Physics "E. R. Caianiello", University of Salerno, via Giovanni Paolo II, Fisciano, Salerno, 84084, Italy. E-mail: adibartolomeo@unisa.it
[b] Tyndall National Institute, University College Cork, Lee Maltings, Dyke Parade, Cork, T12 R5CP, Ireland
[c] School of Chemistry, University College Cork, Cork, Ireland

close to the Fermi level.[29] 2H-$MoTe_2$ has a hexagonal structure and exhibits a narrow indirect bandgap of 0.9 eV in the bulk form and a direct bandgap of 1.1 eV in the few-layer form.[30] In the 1T′–$MoTe_2$ atoms are arranged in a monoclinic structure with in-plane anisotropy, which makes it ideal for applications like polarized photodetectors.[31,32] $MoTe_2$ requires a minimum amount of energy to undergo a transition from 2H to 1T′, 0.035 eV compared to 0.8 eV in the case of MoS_2.[33,34] The transition can be achieved with various techniques, such as strain,[35] temperature[36] or laser pulses.[37]

This phase versatility brings to the forefront one of the main technological challenges in 2D electronics, namely the formation of low-resistance electrical contacts. Large-area $MoTe_2$ FET arrays have been realized by chemically assembling vertical 1T′/2H $MoTe_2$ heterophase structures, where metallic 1T′–$MoTe_2$ acts as the contact and semiconducting 2H-$MoTe_2$ as the channel. This vertical van der Waals contact geometry enables ohmic behavior with strongly reduced contact resistance and field-effect mobilities comparable to exfoliated single-crystal $MoTe_2$, underscoring the suitability of this material for scalable and low-resistance electronic devices.[38]

Due to its relatively small bandgap, $MoTe_2$ can support concurrent electron and hole transport, making it attractive for both electronic and optoelectronic devices. However, this same ambipolar potential is often accompanied by reliability issues, widely linked to Te vacancies and other defect species. Recent research has demonstrated that targeted chemical treatments can ''heal'' Te vacancies and systematically shift threshold voltage and polarity, providing direct evidence that defect engineering is an effective route to improve reproducibility and control in $MoTe_2$ FETs.[39]

Beyond contact engineering, the overall performance of $MoTe_2$-based FETs is further governed by the transport properties of the semiconducting channel itself, which can display ambipolar behaviour depending on a variety of intrinsic and extrinsic factors.[40–42] These include interactions with atmospheric molecules, charge trapping and defects at the oxide interface, as well as intrinsic crystalline point defects within the $MoTe_2$ lattice. Density functional theory (DFT) and Kelvin probe force microscopy (KPFM) prove that physisorbed oxygen molecules on the $MoTe_2$ surface can increase its work function toward p-type behaviour.[43] In contrast, it has been demonstrated that the formation of tellurium vacancies or tellurium adatoms can induce a pronounced n-type conduction.[44]

While sensitivity to defects and environmental factors enables ambipolar transport, it also highlights the need for strategies that allow a more deterministic and controllable modulation of the carrier type. Carrier modulation in ambipolar few-layer $MoTe_2$ FETs has been achieved by employing MgO surface charge transfer doping. The doping process allows for reversible switching of the carrier polarity from p-type to n-type by adjusting the thickness of the MgO layer and the number of $MoTe_2$ layers. Notably, electron mobility in $MoTe_2$ transistors is significantly enhanced, from 0.1 to 20 $cm^2 V^{-1} s^{-1}$, after doping with 37 nm of MgO. This carrier modulation enables high-performance complementary inverters with a high DC gain (>25) and photodetectors, making it a promising approach for the development of advanced electronic and optoelectronic devices based on $MoTe_2$.[45]

However, achieving reliable carrier modulation alone is not sufficient if long-term stability and reproducibility are compromised by environmental degradation. Air-stable monolayer $MoTe_2$ FETs have been demonstrated by encapsulating $MoTe_2$ in hBN and employing a multigate architecture that electrostatically dopes the contacts, enabling low and tunable contact resistance for both electrons and holes. This device concept allows independent control of threshold voltage and contact resistance and has been exploited to realize a complementary inverter and electrostatically defined p–i–n diodes on a single $MoTe_2$ flake, highlighting the suitability of monolayer $MoTe_2$ for integrated logic and optoelectronic circuits.[46]

In this context, despite the significant progress in $MoTe_2$-based electronics, optimizing device performance still requires a deeper understanding of its behavior at the atomic scale. In two-dimensional materials, interfaces are of paramount importance, since the reduced thickness enhances the influence of surface and interfacial phenomena. These effects can critically determine the electrical properties of $MoTe_2$-based devices.

This study investigates electrical transport in back-gated $MoTe_2$ field-effect transistors by combining controlled pressure and temperature experiments. Device characteristics are tracked while pumping down from ambient conditions to high vacuum, and the evolution of the FET figures of merit is discussed together with the role of metal/$MoTe_2$ contacts. Temperature-dependent measurements are subsequently carried out to extract contact-related parameters and to analyze how conduction, subthreshold swing, and threshold voltage evolve with temperature. Vacuum annealing is employed to probe defect dynamics and their impact on the electrical response. Finally, measurements conducted while progressively increasing the pressure from vacuum are used to assess how surface exposure affects transport through adsorption processes. Each of the mechanisms proposed on the basis of experimental results, is supported by DFT simulations. Unlike previous studies,[47,48] here we perform systematic temperature and pressure sweeps to shed light on the different phenomena governing electrical transport in the material. These results, combining experimental measurements and DFT-based simulations, provide a consistent framework to disentangle the contribution of contacts, traps, and surface adsorbates in $MoTe_2$-based devices.

2. Materials and methods

Fig. 1a shows the hexagonal crystalline structure of a monolayer 2H-$MoTe_2$ from both top and side views. The structure consists of an atomic layer of molybdenum atoms (blue) located between two layers of tellurium atoms (purple). The $MoTe_2$ flake was used as the channel of a FET, fabricated as described in the following. Flakes of 2H-$MoTe_2$ are mechanically exfoliated and transferred over a substrate of highly p-doped silicon wafer, which serves as the gate of the FET. The gate dielectric

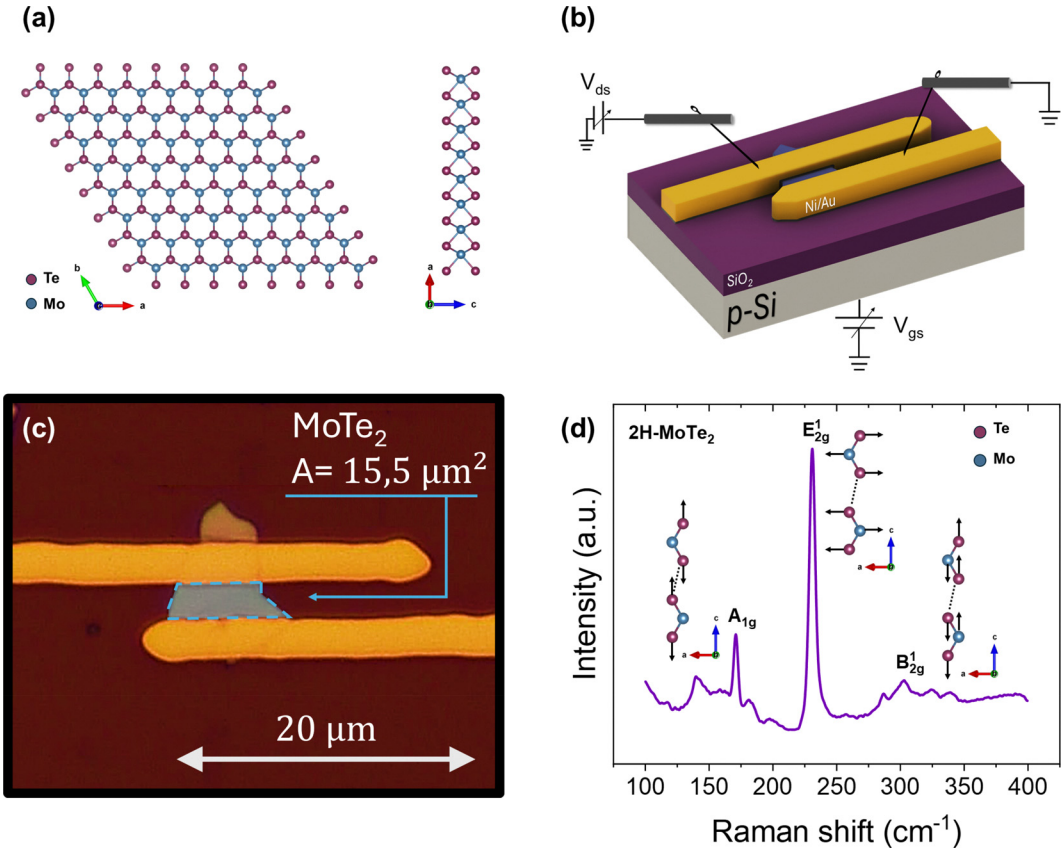

Fig. 1 Device structure and morphology. Crystalline structure of monolayer 2H-$MoTe_2$ from different perspectives (a). Three-dimensional schematic of the device (b). Optical image of the device, the dashed line highlights the active area of the $MoTe_2$ flake (c). Raman spectrum of the 2H-$MoTe_2$ flake on a Si/SiO_2 substrate (d).

consists in a layer of 85 nm silicon dioxide (SiO_2) thermally grown on the p-Si. After the flake transfer, Ni/Au (20 nm/150 nm) metallic contacts are formed by photolithography, electron-beam metal evaporation, followed by the standard lift-off process. A three-dimensional schematic of the final device is reported in Fig. 1b. The two metallic contacts on top of the $MoTe_2$ flake are used as the drain and the source of the transistor, while the gate voltage is applied to the p-Si substrate. The optical top-view image of the device is shown in Fig. 1c. The active area of the $MoTe_2$ flake, corresponding to about 15.5 μm^2, is highlighted in light blue. The channel length and width, *i.e.* the average linear dimensions of the active area, correspond to $L = 2.23$ μm and $W = 6.95$ μm, respectively. Fig. 1d shows the Raman spectrum of the 2H-$MoTe_2$ flake, acquired using a Horiba XploRA plus Raman microscope with an EMCCD detector and 532 nm laser excitation. Three main peaks are evident at 170 cm^{-1}, 230 cm^{-1} and 288 cm^{-1}, which correspond to the A^1_g, E^1_{2g} and B^1_{2g} vibrational modes respectively.[49–51] These modes consist of vibrations of tellurium and molybdenum atoms, as illustrated in Fig. 1d. The B^1_{2g} peak is absent in monolayers and in bulk $MoTe_2$, but becomes Raman-active in few-layer flakes due to the breaking of translational symmetry.[52] Specifically, its intensity is reported to be maximal for bilayers and to decrease with increasing thickness.[53] A minor peak is also detected at 139 cm^{-1}, which can be attributed to a second-order Raman process, as observed in other dichalcogenides.[54,55] The intensity ratio between the B^1_{2g} and E^1_{2g} peaks is ~1.5, while frequency separation between these two modes is ~61 cm^{-1}, indicating a few-layer (approximately 3–5 layers) $MoTe_2$ flakes.[49–51]

The electrical measurement of the system is conducted using a Keithley semiconductor characterization system 4200-SCS in combination with a Lakeshore TTPX cryogenic probe station. The station is equipped with a rotative pump and a turbomolecular pump, which enable two different vacuum levels inside the probe chamber. The reported electrical characterization refers to a single representative device; however, multiple devices were fabricated within the same batch and measured under the same experimental protocol. Consistent behaviour and reproducible results were observed across all measured devices.

The band structure calculations were performed within the framework of density functional theory (DFT), employing a linear combination of numerical atomic orbital (LCAO) basis sets as implemented in QuantumATK.[56] Norm-conserving pseudopotentials from the PseudoDojo library were used in combination with medium-quality basis sets.[57] Brillouin zone integration was carried out using the Monkhorst–Pack *k*-point

sampling scheme,[58] with a density of approximately 10 *k*-points per Å^{-1}. A real-space grid energy cutoff of 115 Hartree was applied.

Structural optimizations were conducted using the Perdew–Burke–Ernzerhof (PBE) exchange–correlation functional within the generalized gradient approximation (GGA), while van der Waals (vdW) interactions were accounted for *via* the Grimme DFT-D3 dispersion correction method.[59] Although GGA is known to underestimate band gaps compared to hybrid functionals such as HSE,[60,61] this limitation does not affect the conclusions, as all calculations employed the same functional consistently. All geometries were relaxed using the limited-memory Broyden–Fletcher–Goldfarb–Shanno (L-BFGS) algorithm until the maximum force on any atom was less than 0.02 eV Å^{-1}.

To study the impact of physisorbed oxygen molecules, a slab model of 2H-$MoTe_2$ was constructed using equilibrium lattice parameters of a = 3.52 Å and c = 13.96 Å, representing the hexagonal phase.[61,62] Both bulk and thin-film systems were considered, including structures with molybdenum (Mo) and tellurium (Te) vacancies to investigate their effects on electronic properties. To analyse the effects of the oxygen adsorbate on the $MoTe_2$ surface, a single oxygen molecule on a 5 × 5 × 1 three-layer $MoTe_2$ supercell, corresponding to a density of $\approx 4 \times 10^{13}$ cm^{-2}, was considered.

To prevent the emergence of artificial electric fields due to the asymmetry introduced by the O_2 molecule adsorbed on one side of the slab, Neumann and Dirichlet boundary conditions were applied to the O_2-covered and bare surfaces, respectively. This approach provides an alternative to standard dipole correction methods in slab-based simulations.[63]

3. Results and discussion

The electrical characterization was conducted at room temperature and in the dark. Fig. 2a shows the IV curve, on a semi-logarithmic scale, for three different pressures: 1 bar, 10 mbar, and 10^{-3} mbar (violet, blue, and green curves respectively), and with a grounded gate. Regardless of the pressure, the current does not increase linearly with the applied voltage, either positive or negative, as shown in the inset, which displays the IV curve under 1 bar pressure in a linear scale. Such behaviour is typical of a metal–semiconductor interface with a Schottky barrier. In the present case, nickel contacts have a work function $\Phi_M \approx 5.0$ eV, whereas the 2H-$MoTe_2$ work function Φ_S can be higher than 5.6 eV,[64] and a Schottky barrier for holes can originate after Fermi level alignment, being $\Phi_M < \Phi_S$.[65,66] For the device under study, measured in a standard two-probe configuration, each contact likely forms a Schottky junction and hence a potential barrier for hole injection. Therefore, the system can be modeled by two back-to-back Schottky diodes: when a certain voltage is applied, one junction is forward-biased while the other is reverse-biased.[67,68] In this kind of configuration, the measured current is predominantly governed by the reverse-biased junction, so each branch of the IV curve effectively reflects reverse conduction, at both positive and negative biases. Nevertheless, the barrier height depends on the applied bias voltage, for instance, through image force lowering, so the current does not saturate at either positive or negative bias. Within the thermionic emission model, each branch of the IV curve can be fitted using the equation:[69]

$$I_d = I_0 \exp\left(\frac{qV}{nk_BT}\right)\left[1 - \exp\left(-\frac{qV}{k_BT}\right)\right] \quad (1)$$

$$I_0 = AA^*T^2 \exp\left(-\frac{\Phi_B}{k_BT}\right) \quad (2)$$

where I_0 is the reverse saturation current, q is the elementary charge, n is the ideality factor of the junction, k_B is the Boltzmann constant, T is the absolute temperature, Φ_B is the voltage dependent Schottky barrier height, A is the contact area, and A^* is the so-called Richardson constant. The results of the fit (red and orange solid lines) are reported in the inset of Fig. 2a. Moreover, the increase in current observed under vacuum conditions can be attributed to a reduction of the hole Schottky barrier at the contacts,[70,71] and possibly to a decrease in the channel scattering rate. These effects outweigh the reduction in conductivity resulting from the lower p-doping level caused by the desorption of adsorbed molecules in a vacuum.

The current flowing within the channel can be modulated by the gate voltage V_{gs}, as shown in Fig. 2b, which shows the transfer characteristics at a drain bias of V_{ds} = 500 mV, measured in air (1 bar) and under vacuum (10 mbar and 10^{-3} mbar). The gate current I_g was monitored throughout the measurements and remained below 10^{-10} A over the relevant bias range. Therefore, the recorded transfer characteristics are not affected by gate leakage. Independent of the pressure, the material shows a p-type behaviour, as evidenced by the increase in current under increasingly negative gate bias. This behaviour is consistent with p-type doping expected from Te and, predominantly, Mo vacancies, which are predicted to contribute to the hole concentration based on DFT calculations (Fig. 2c and d). Indeed, the simulation shows that these vacancies shift the Fermi level toward lower energies, rendering the crystal p-type, while simultaneously introducing defect states within the bandgap. The transistor current arises from the modulation of hole concentration in the channel, which is lowered at negative gate biases. The gate voltage sweeping direction strongly affects the current, resulting in a pronounced hysteresis. This behaviour is common in 2D materials and is strongly influenced by the molecules adsorbed on the channel's surface and by defects within the material.[72,73] The holes field effect mobility can be computed according to the equation:

$$\mu_p = \frac{L}{WV_{ds}C_{ox}}\left|\frac{dI_{ds}}{dV_{gs}}\right| \quad (3)$$

where L and W are the channel dimensions previously defined, $C_{ox} = 4.06 \times 10^{-8}$ F cm^{-2} is the oxide capacitance, and the derivative of the drain current with respect to the gate voltage is computed in the linear region of the positive branch of the

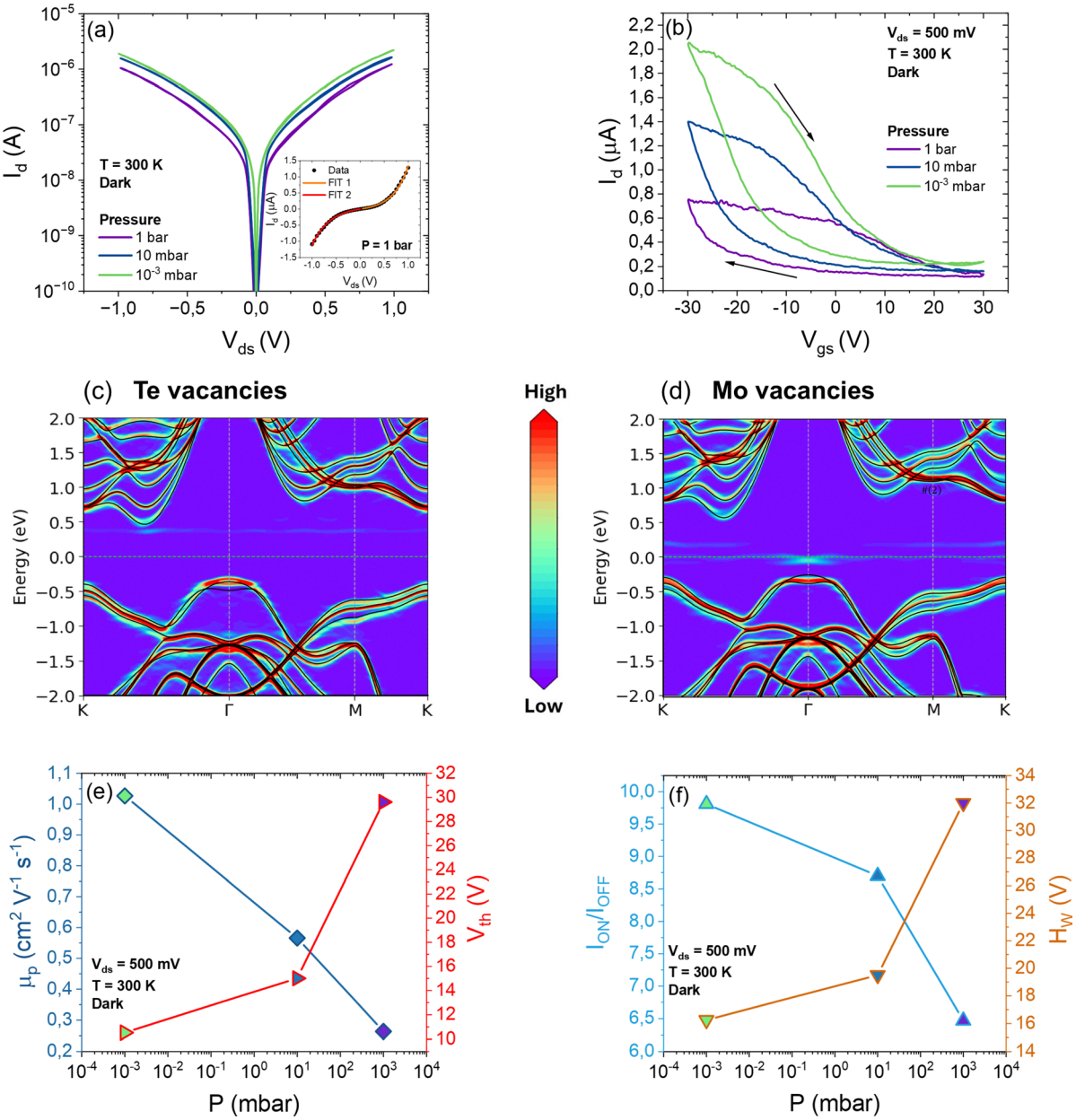

Fig. 2 Electrical characterization at different pressures. IV curves on a semi-logarithmic scale measured at three different pressures and with the grounded gate; the inset shows the 1 bar IV curve on a linear scale with an exponential fit for each branch (a). Transfer characteristics on a linear scale for V_{ds} = 500 mV and different pressures (b). Unfolded band structure of the $MoTe_2$ film with Te (c) and Mo (d) vacancies, shown as contour plots of the total spectral weight intensity. The primitive-cell band structure of pristine $MoTe_2$ is overlaid as black solid lines. The localized states associated with Te and Mo vacancies appear close to the conduction band edge (Te vacancy) and the valence band edge (Mo vacancy). The zero of energy corresponds to the Fermi level. Field effect mobility (blue *y*-axis) and threshold voltage (red *y*-axis) extracted from the transfer curves (e). I_{ON}/I_{OFF} ratio (light blue *y*-axis) and hysteresis width (brown *y*-axis) extracted from the transfer curves (f). All measurements in a, b, e, and f were conducted in the dark and at room temperature.

transfer curve (negative to positive voltage sweep) through a linear fit. The threshold voltage, V_{th}, is then determined by linear extrapolation of the fitted transfer curve. The same procedure is applied to all transfer curves in this study; however, the linear fitting region depends on the measurement conditions. Therefore, the V_{gs} fitting window is selected case by case, as a fixed window would not be suitable.[74–76] At ambient pressure, the drain current varies between about 0.12 μA (at V_{gs} = +30 V) and 0.75 μA (at V_{gs} = −30 V), hence the I_{ON}/I_{OFF} ratio is 6.47 under these conditions. Hysteresis can be quantified by its maximum width H_W, which is equal to 32 V at ambient temperature and pressure. Under the same conditions, the hole mobility is μ_p = 0.26 $cm^2\ V^{-1}\ s^{-1}$, while the threshold voltage is V_{th} = 29.62 V. The low mobility is consistent with the presence of intrinsic defects in the material, such as Te or Mo. Moreover, since the electrical characterization is

performed in a two-probe configuration, the extracted field-effect mobility includes the contribution of the contact resistance R_c, which adds in series to the channel sheet resistance R_{sh}.[77] As a result, the absolute mobility values can be underestimated when the transport is partially contact-limited. Nevertheless, all measurements were carried out using the same device geometry and the same protocol while varying pressure and temperature; therefore, the reported pressure/temperature trends remain meaningful and are corroborated by consistent variations in other parameters. Fig. 3e reports the effect of pressure on μ_p (blue) and V_{th} (red). In agreement with the previous observations, current is larger and shows minor fluctuations under vacuum, possibly due to the decrease in SBH and in scattering rate. This could determine a higher mobility (up to 1.03 $cm^2\ V^{-1}\ s^{-1}$ at $P = 10^{-3}$ mbar), corresponding to a steeper curve, at lower pressure. The reduction of adsorbed air molecules determines a left-shift of the threshold voltage to 10.52 V. This behavior will be analyzed in detail later in the discussion. The effect of pressure on I_{ON}/I_{OFF} and H_W is made clear in Fig. 2f. The I_{ON}/I_{OFF} ratio increases up to 9.81, while the hysteresis width decreases in a vacuum, indicating that part of the hysteresis is related to surface-adsorbed molecules. Under vacuum, the reduced adsorbate coverage typically mitigates these surface-related traps, leading to a narrower hysteresis. However, the two branches of the curve remain separated, with H_W = 16.25 V at $P = 10^{-3}$ mbar, suggesting that additional trapping centers are still active. To check the device-to-device variability, more than 10 similar devices were examined under comparable measurement conditions, namely under vacuum (10^{-3} mbar), in the dark, and at room temperature. Across this set of devices, the extracted field-effect mobility was found to range from 0.59 $cm^2\ V^{-1}\ s^{-1}$ up to 2.25 $cm^2\ V^{-1}\ s^{-1}$, the hysteresis width from 17 V to 24 V, and the I_{ON}/I_{OFF} ratio between 6 and 9. In addition, the current levels were found to be nearly the same across the investigated devices, with a maximum current of about 3.3 μA reached at $V_{gs} = -30$ V and $V_{ds} = +0.5$ V. Moreover, we highlight that the overall trends of the IV characteristics remain consistent with those discussed throughout the manuscript, providing further support for the interpretation of the transport behavior of $MoTe_2$ transistors.

This residual hysteresis is consistent with intrinsic trap states at the channel/dielectric interface and defect-related states within $MoTe_2$, which are not affected by desorption. An estimate of this trap population can be obtained from the hysteresis width, which is related to the net trapped charge and the corresponding effective trap density n_t as:[78,79]

$$n_t = \frac{\Delta Q_t}{q} = \frac{C_{ox} H_W}{q} \quad (4)$$

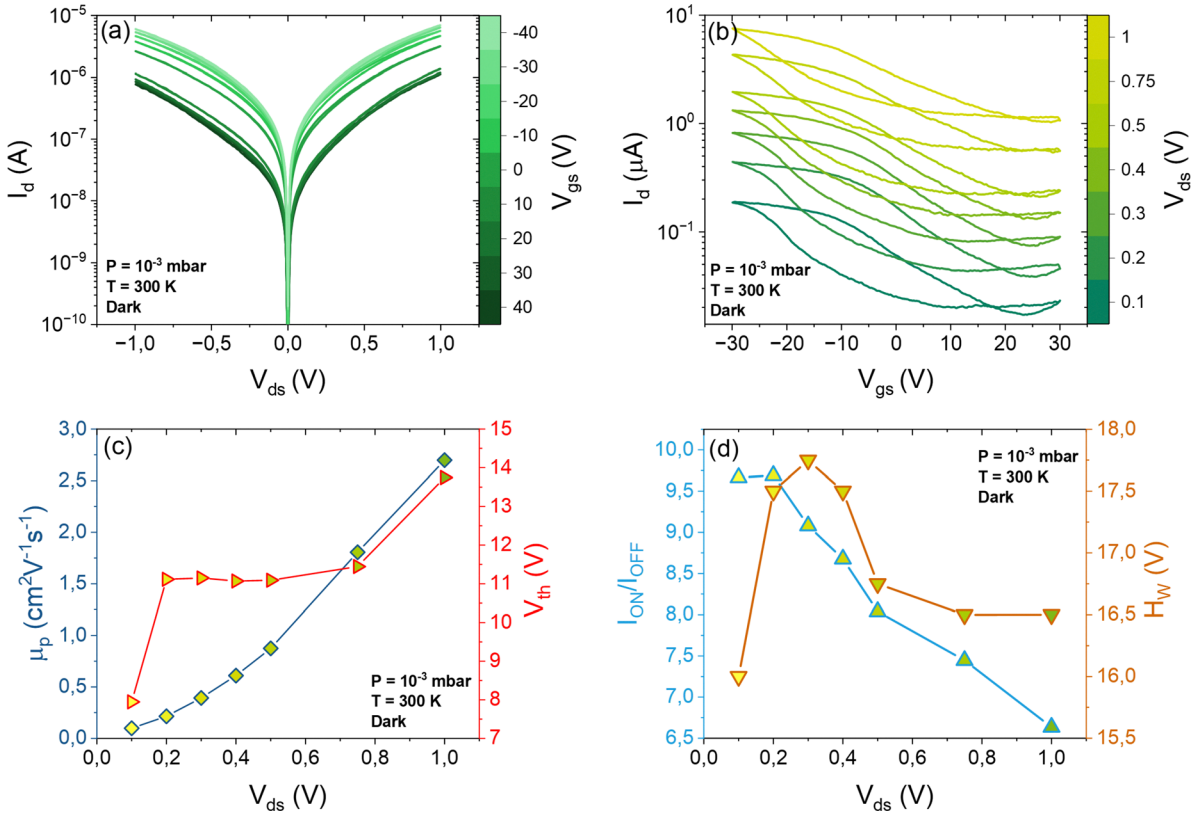

Fig. 3 Electrical characterization in a vacuum. Output characteristics on a semi-logarithmic scale at $P = 10^{-3}$ mbar (a). Transfer characteristics on a semi-logarithmic scale for increasing values of V_{ds} at $P = 10^{-3}$ mbar (b). Field effect mobility (blue y-axis) and threshold voltage (red y-axis) extracted from the transfer curves as a function of the drain bias (c). I_{ON}/I_{OFF} ratio (light blue y-axis) and hysteresis width (brown y-axis) extracted from the transfer curves as a function of the drain bias (d). All measurements were conducted in the dark and at room temperature.

Table 1 Comparison between the present study and representative reports from the literature[80–83]

Ref.	Contacts	Layer(s)	Dielectric	Environment	μ_p ($cm^2\ V^{-1}\ s^{-1}$)	I_{ON}/I_{OFF}	H_W (V)	SBH (meV)
Present work	Ni/Au	3–5	SiO_2	Vacuum ($P = 10^{-3}$ mbar)	1.03	9.81	16.25	~37.5
80	Ni	Multilayer	SiO_2	Ambient pressure	0.55	~9	~45	150
81	Ti/Au	Multilayer	SiO_2	Ambient pressure	10^{-2}	10^2	—	—
82	Cr/Au	4	SiO_2	Vacuum ($P = 10^{-2}$ mbar)	—	10^3	—	—
83	Ti/Au	30	SiO_2	Ambient pressure	6.4	10^3	—	120

where C_{ox} is the gate-oxide capacitance per unit area, H_W is the hysteresis width defined above, and q is the elementary charge. Using this relationship, an effective trap density of $n_t \sim 10^{12}\ cm^{-2}$ is estimated at $P = 10^{-3}$ mbar.

Table 1 benchmarks the key figures of merit of the present $MoTe_2$ FETs against representative reports from the literature.[80–83] The measured hole mobility is comparable to that reported for similar devices. Concerning the I_{ON}/I_{OFF} ratio, similar values are found in other $MoTe_2$ devices employing Ni-based contacts under similar dielectric platforms, whereas a larger I_{ON}/I_{OFF} ratio is often obtained with different contact schemes, depending on device geometry and measurement conditions.

This comparison suggests that the relatively limited modulation observed in the present study may be influenced by contact injection and trap-related doping. In particular, Ni contacts are expected to favor hole injection in $MoTe_2$, reducing the effective barrier for holes and increasing the residual conductance in the nominal "OFF" state, which naturally limits the achievable I_{ON}/I_{OFF}. In addition, in-gap trap states and vacancy-related defects can increase the background carrier density and contribute to hysteresis, further raising the off-current and reducing the modulation depth. Consistently, devices measured in a vacuum show a reduced hysteresis compared to ambient conditions, supporting the role of adsorbates as an additional, pressure-dependent contribution to the trap landscape.

Several strategies can be adopted to enhance the I_{ON}/I_{OFF} ratio and mobility in these devices. Mainly, improved fabrication protocols and post-fabrication treatments aimed at reducing the density of electrically active defects are expected to strengthen electrostatic channel control.[84,85] In addition, encapsulation can suppress adsorbate-induced doping and trapping, thereby reducing hysteresis and improving the separation between ON and OFF states.[86,87] Finally, contact engineering, such as using metallic 1T′–$MoTe_2$ contact phases, may mitigate contact-limited injection and further increase the achievable modulation.[87]

Nevertheless, the moderate performances as FET do not affect the scope of this study, which focuses on clarifying the role of defects and trap states in charge transport.

Fig. 3a shows the output curves in a high vacuum (10^{-3} mbar) obtained by stepping the gate voltage from +40 V down to −40 V in steps of −10 V. The p-type behavior is confirmed; indeed, a larger current is obtained when a negative gate voltage is applied, independently of the applied bias to the drain. The exponential trend with V_{ds} remains for each value of the gate voltage, with a slight modification of the shape of the curve, which is expected since the gate voltage affects the energetic bands of the material in the channel as well as in the contact region.[65] The modulation of the channel current is affected also by the drain bias as shown by the transfer curves at different V_{ds}, between 0.1 V and 1 V in Fig. 3b. Being the contact of Schottky type, the current grows exponentially at higher V_{ds}, hence the transfer curves measured at larger drain biases are shifted upward. The effect of the bias on the mobility and threshold voltage is clarified in Fig. 3c. The mobility increases with V_{ds}, reaching a maximum value of 2.70 $cm^2\ V^{-1}\ s^{-1}$ for $V_{ds} = 1$ V, which can be attributed to reduced contact resistance and a transition from trap-limited transport to a more delocalized transport regime at higher electric fields. For higher values of V_{ds}, the threshold voltage is also subjected to a slight increase, switching from 7.94 V at $V_{ds} = 0.1$ V up to 13.75 V at $V_{ds} = 1$ V. This behaviour can be explained by the lowering of the effective drain Schottky barrier at higher bias, which requires a more positive gate voltage to fully deplete the channel of holes and turn the transistor off. Finally, Fig. 3d reports the dependence of I_{ON}/I_{OFF} and H_W on V_{ds}. The separation between the ON and OFF states of the transistor is reduced as long as V_{ds} increases. This behaviour can be ascribed to an enhancement of the OFF-state current, due to drain-induced barrier lowering and trap-assisted conduction. The maximum hysteresis width exhibits a non-monotonic dependence on the drain bias: it initially increases as the bias is raised and subsequently decreases at higher bias values. A possible explanation is the following: at high drain voltages, the stronger lateral electric field enhances charge trapping and detrapping in the dielectric and at the channel interfaces, leading to a widening of the hysteresis. At higher drain bias, however, trap occupancy tends to saturate and diminish the effective threshold shift between the forward and backward sweeps, resulting in a reduced hysteresis width.[79,88–90]

i. Temperature-dependent behavior

Temperature measurements were conducted, in the dark and at $P = 10^{-3}$ mbar, to better understand the transport properties of $MoTe_2$. Fig. 2a shows the IV curves at $P = 10^{-3}$ mbar for different temperatures, increasing from 77 K up to 400 K. At higher temperatures, the increased kinetic energy of charge carriers enhances hole injection at the contacts and the current increases. The plot shows a small asymmetry that gradually diminishes with increasing temperature, consistent with thermionic conduction.[70] Moreover, as the temperature increases, the available thermal energy frees charge carriers from defect traps or localised states within the material. This leads to a higher concentration of mobile carriers and, consequently, a rise in electrical conductance. This kind of trend is

characteristic of semiconductors, in which electrons in the valence band acquire sufficient energy to be transferred into the conduction band through intragap states, causing the conductivity to grow with increasing temperature.[91] The temperature-dependent analysis is useful to extract the Schottky barrier heights (SBHs) at the two metal–semiconductor interfaces. To do this, one can use the temperature dependence of the zero-bias current, I_0, and construct the Richardson plot, which is typically linear, according to the equation:[70,91]

$$\ln\left(\frac{I_0}{T^2}\right) = \ln(AA^*) - \frac{\Phi_B}{k_B T} \quad (5)$$

I_0 can be extracted as the intercept of the linear fit of either the forward or reverse bias region of the semi-logarithmic IV curve. The analysis was carried out for both positive and negative values of the drain biases. Fig. 4b reports the Richardson plot computed for $V_{ds} < 0$. The thermionic conduction over the Schottky barrier is confirmed by the linear trend of the Richardson plot, as shown by the linear fit (black dashed line), for temperatures higher than 200 K. At lower temperatures, the deviation from the expected behaviour arises from the onset of conduction mechanisms other than thermionic emission, such as tunnelling or recombination. Moreover, it suggests the presence of spatially inhomogeneous barrier heights and

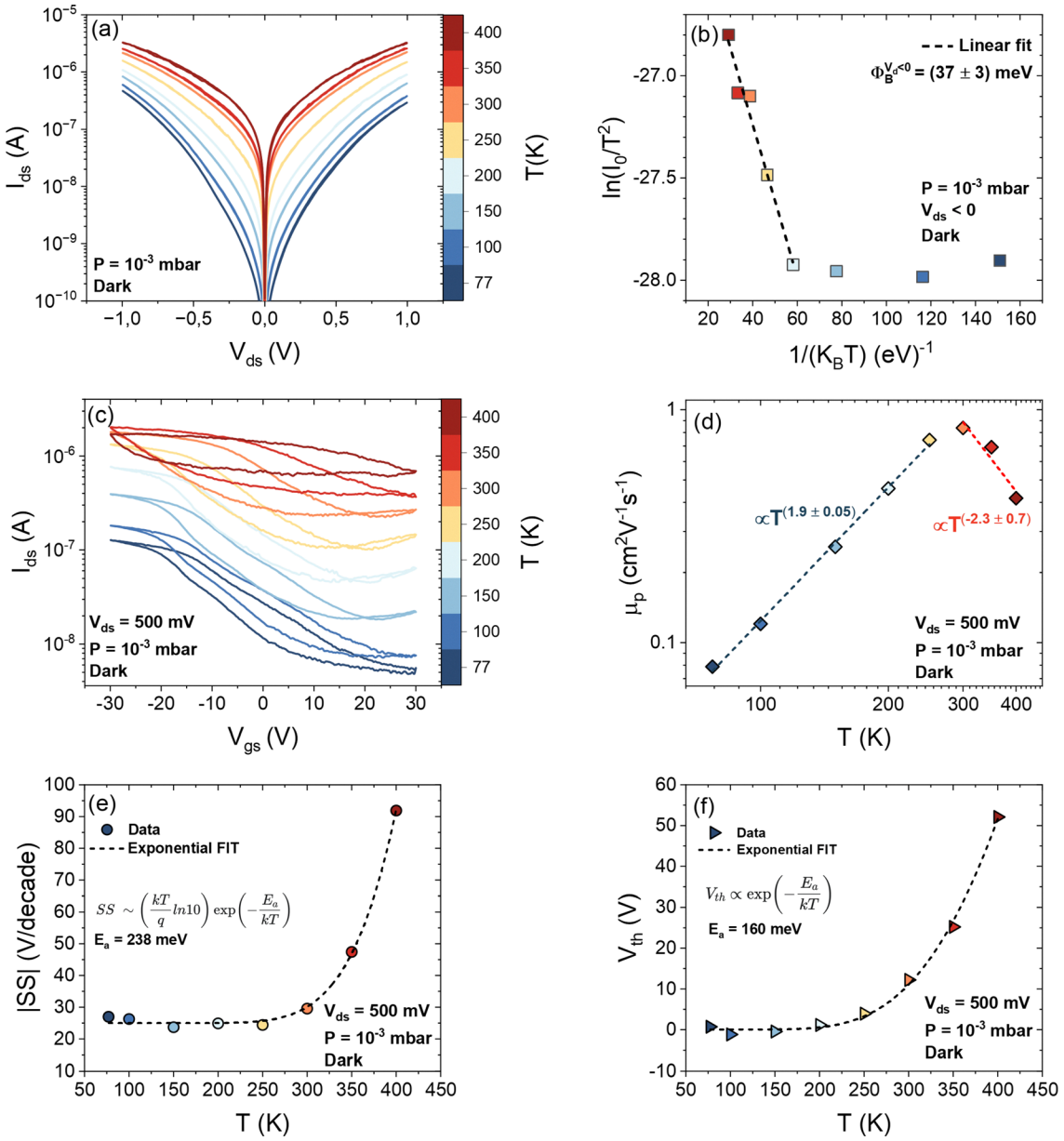

Fig. 4 Electrical characterization as a function of temperature. IV curves measured at different temperatures from 77 K to 400 K (a). Corresponding Richardson plot for positive drain biases, $V_{ds} > 0$; the black dashed line is a linear FIT (b). Transfer characteristics at V_{ds} = 500 mV for temperatures from 77 K to 400 K (c). Field-effect mobility as a function of temperature on a double-logarithmic scale; the blue and red dashed lines indicate linear fits (d). |SS| (e) and V_{th} (f) as a function of temperature with exponential fits (black dashed lines). All measurements were conducted in the dark and at $P = 10^{-3}$ mbar.

potential fluctuations at the interface, resulting in regions with both low and high barrier heights.[92–94] Indeed, according to the model proposed by Werner–Güttler,[95] in the presence of inhomogeneities, the barrier height is treated as a Gaussian distribution with mean value $q\,\phi_B^0$ and standard deviation σ. At low temperature, charge transport is dominated by preferential conduction through regions with locally reduced barrier height, so the extracted effective barrier $q\,\phi_B^{eff}$ deviates from the mean value and the Richardson analysis no longer yields a single, temperature-independent barrier. As temperature increases, carriers gain sufficient thermal energy to sample a larger portion of the distribution, and $q\,\phi_B^{eff}$ approaches the mean barrier $q\,\phi_B^0$. Therefore, the SBH extracted from the high-temperature linear regime ($T \geq 200$ K), is reliable as an effective/mean barrier representative of the room-temperature interface under the considered bias polarity. The SBHs, extracted as the slopes of the linear fits, are only slightly different with $\Phi_B^{V_d>0} = (38 \pm 6)$ meV and $\Phi_B^{V_d<0} = (37 \pm 3)$ meV. The low and similar Schottky barriers at the two contacts are expected, given the relatively high channel current and almost symmetric IV curves. This value is smaller than what would be expected from a simple comparison of Φ_M and Φ_S, indicating that the contact does not follow the ideal Schottky–Mott limit. Instead, the measured barrier suggests that the Ni Fermi level is effectively close to the $MoTe_2$ valence-band edge at the interface. This kind of reduced effective barrier can arise from interface dipoles and charge transfer, the presence of interfacial (gap) states, and the resulting Fermi-level pinning, which strongly modifies the local band alignment compared to the vacuum-level estimate.[96–99] Moreover, the presence of interface states and defects can lead to Fermi-level pinning, strongly reducing the sensitivity of the barrier height to the metal work function and yielding much smaller effective barriers than those expected from the Schottky–Mott estimate.[100–102] Finally, considering the presence of barrier inhomogeneity and potential fluctuations, current preferentially flows through locally low-barrier patches, which can further reduce the apparent barrier height compared to a uniform-barrier picture.[70,95]

Fig. 4c reports the transfer curves at V_{ds} = 500 mV for temperatures from 77 K up to 400 K. Consistently with the IV curves, current increases with temperature. Specifically, the trap and localized states, which are progressively emptied as temperature increases due to thermal activation, are more populated when a positive gate bias is applied. Therefore, the temperature-induced increase in current is particularly pronounced when the transistor is in the OFF state. As a result, the OFF-state current rises with temperature, leading to a corresponding reduction in I_{ON}/I_{OFF} ratio. The p-type behaviour is preserved for each value of temperature in the considered range.

The temperature dependence of the hole field-effect mobility is reported in the double-logarithmic plot in Fig. 4d. μ_p exhibits a power-law increase with temperature from 77 K to 300 K, after which it transitions to a power-law decay. This behaviour can be attributed to distinct scattering mechanisms. At low temperatures, charge transport is mainly limited by scattering from ionized impurities in the material; in this regime, the mobility scales with temperature as $\mu_p \propto T^{\frac{3}{2}}$; in contrast, mobility decreases like $\mu_p \propto T^{-\frac{3}{2}}$ at higher temperatures because of acoustic phonon scattering which becomes the dominant mechanism. From a linear fit in the double-logarithmic plot the exponents can be extracted, obtaining $\mu_p \propto T^{(1.9\pm0.05)}$ for $T < 300$ K and $\mu_p \propto T^{(-2.3\pm0.7)}$ for $T > 300$ K. These values are consistent with the two mentioned mechanisms which remain the main ones, however, the slow deviation from theoretical values is to impute to other scattering mechanisms and is consistent with results found in the literature.[65,103,104] The subthreshold swing (SS) was extracted from the transfer as $SS = \left|\frac{d \log I_d}{d V_{gs}}\right|^{-1}$ and its trend as a function of the temperature is reported in Fig. 4e. Typically, one expects the SS to scale linearly with the temperature, according to the equation:[65]

$$SS = \left(\frac{k_B T}{q} \ln 10\right)\left(1 + \frac{q^2 D_{it}}{C_{ox}}\right) \quad (6)$$

where D_{it} is the density of interface defects and C_{ox} is the oxide capacitance. However, in the case of study, the experimental fit (black dashed lines) demonstrates that the trend is exponential. This can be attributed to band tails, *i.e.* to defect states near the band edges that decay exponentially into the band gap, resulting in ref. 105–107:

$$SS \approx \left(\frac{k_B T}{q} \ln 10\right) e^{-\frac{E_a}{k_B T}} \quad (7)$$

where E_a is the activation energy. The equation is valid for $1 \ll \frac{q^2 D_{it}}{C_{ox}}$, which is reasonable considering the device under study. The activation energy extracted from the fit is E_a = 238 meV. This value is very close to others found in the literature for $MoTe_2$ and gives the extension of the band tail, that is, of the energy range of defect states above the valence band.[108] A similar exponential trend in temperature was observed for the threshold voltage, as visible in Fig. 4f. However, in this case the activation energy, extracted through an exponential fit (black dashed line in figure) is E_a = 160 meV. Despite the smaller energy, the exponential behaviour confirms the role of the $MoTe_2$ band tail in the switching behaviour of the transistor.

ii. Defects study

The gate modulation is affected by thermal annealing, as demonstrated in Fig. 5a, which shows the transfer curve at $P = 10^{-3}$ mbar before and after heating the device for 1 h at 400 K. It is clear that after the annealing the current is much smaller over the entire V_{gs} range considered, with a reduction of the I_{ON}/I_{OFF} ratio from 9.81 to 3.11. Holes remain the majority charge carriers, even though their mobility is decreased from μ_p = 1.03 cm^2 V^{-1} s^{-1} to μ_p = 0.35 cm^2 V^{-1} s^{-1}. It is also observed that a slight ambipolar behavior appears after the annealing, with an electron mobility of μ_n = 0.06 cm^2 V^{-1} s^{-1}.

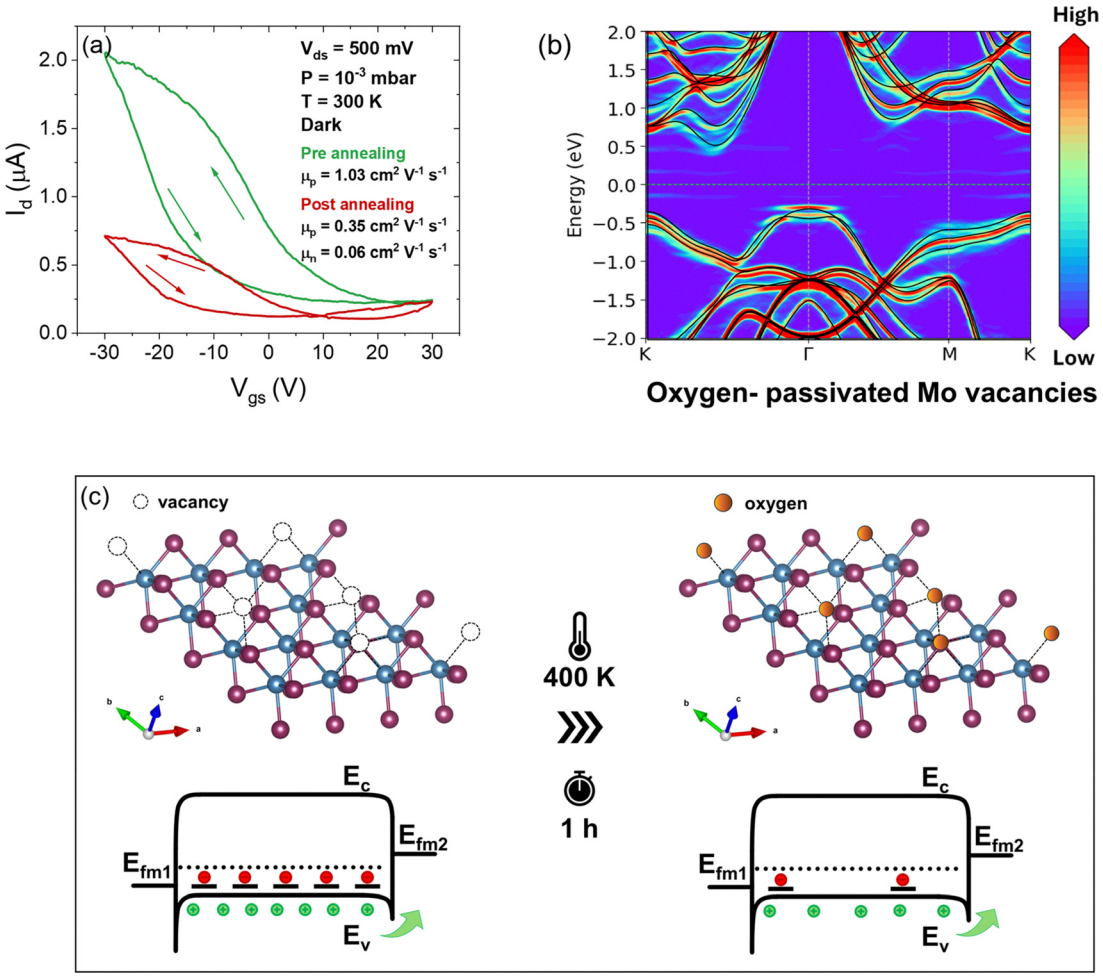

Fig. 5 Electrical characterization as a function of pressure. Transfer characteristics under dark conditions, at V_{ds} = 500 mV, T = 300 K and $P = 10^{-3}$ mbar, before (green curve) and after (red curve) thermal annealing at 400 K for 1 h (a). Unfolded band structure of an oxygen-passivated Mo vacancy in $MoTe_2$. Oxygen passivation reduces the vacancy-induced p-type doping and associated localized states. Black solid lines represent the primitive-cell band structure of pristine $MoTe_2$. The zero of energy corresponds to the Fermi level (b). Schematic illustration of the effect of annealing on the device surface and the corresponding band diagram (c).

This behaviour is consistent with the ambipolar Schottky-barrier transport widely reported in $MoTe_2$ FETs and likely reflects the strong suppression of p-type conduction (reduced hole density/modified interfacial states), which makes the otherwise weaker electron contribution observable.[41,61,109] Concurrently, the threshold voltage exhibits a small left shift from 10.0 V to 8.7 V. To appropriately explain this phenomenon, several observations must be considered. Desorption of surface contaminants can reduce current by diminishing the p-doping effect of O_2 and H_2O molecules, but this is often offset by an increase in current due to a reduction of the hole Schottky barrier at the contacts[70,71] and decreased adsorbate-induced scattering. The pronounced decrease in current and the suppression of p-type transport after annealing suggest a mechanism beyond desorption. As both Te and Mo vacancies contribute to the p-doping of the material, their passivation may suppress the doping level and contribute to the observed reduction in conductivity. Moreover, a structural phase change is unlikely under the adopted thermal budget, as it is typically induced only by annealing at much higher temperatures ($T > 1000$ K).[110,111] Finally, oxygen-related processes in $MoTe_2$ are known to be strongly defect-assisted: vacancies can act as reactive sites that promote oxygen bonding/intercalation, thereby modifying the interfacial potential landscape and the distribution of in-gap states.[112–114] Therefore, prior to thermal annealing, Mo and Te vacancies could introduce acceptor-like states which capture electrons from the valence band and release holes. At equilibrium this would result in a pronounced p-type behavior. The thermal energy provided during annealing would promote oxidation and passivation of the Te and Mo vacancies, reducing the concentration of defect-induced holes, consistent with the DFT calculations shown in Fig. 5b. Annealing possibly modifies the distribution of in-gap trap states, as schematically illustrated by the band model in Fig. 5c. In this scenario, before annealing, vacancies increase the hole density (left-side of the image), while as these defects become passivated, the density of the acceptor-like trap states is reduced, leading to a partial suppression of hole conduction and the

emergence of weak electron transport (right-side of the image). The observed small shift in the threshold voltage after the annealing can be attributed to the modification of the charges in the trap states.[65]

To further confirm this explanation, the device was studied during the adsorption process, sweeping from 10^{-3} mbar to atmospheric pressure. After a 30 minutes stabilization at each step to allow adsorption, IV and transfer curves were measured. This waiting time was adopted as a conservative criterion; indeed, repeated measurements after each pressure change showed that the device response reached a stable state within this interval. Fig. 6a shows the IV curves obtained for different pressure values during this sweep. The Schottky behavior is maintained independently of pressure, which is expected since it is attributed to the metal/semiconductor interface. At first, the current becomes lower while increasing the concentration of air molecules and then starts to increase, as shown by the conductance plot in Fig. 6b. Specifically, conductance was

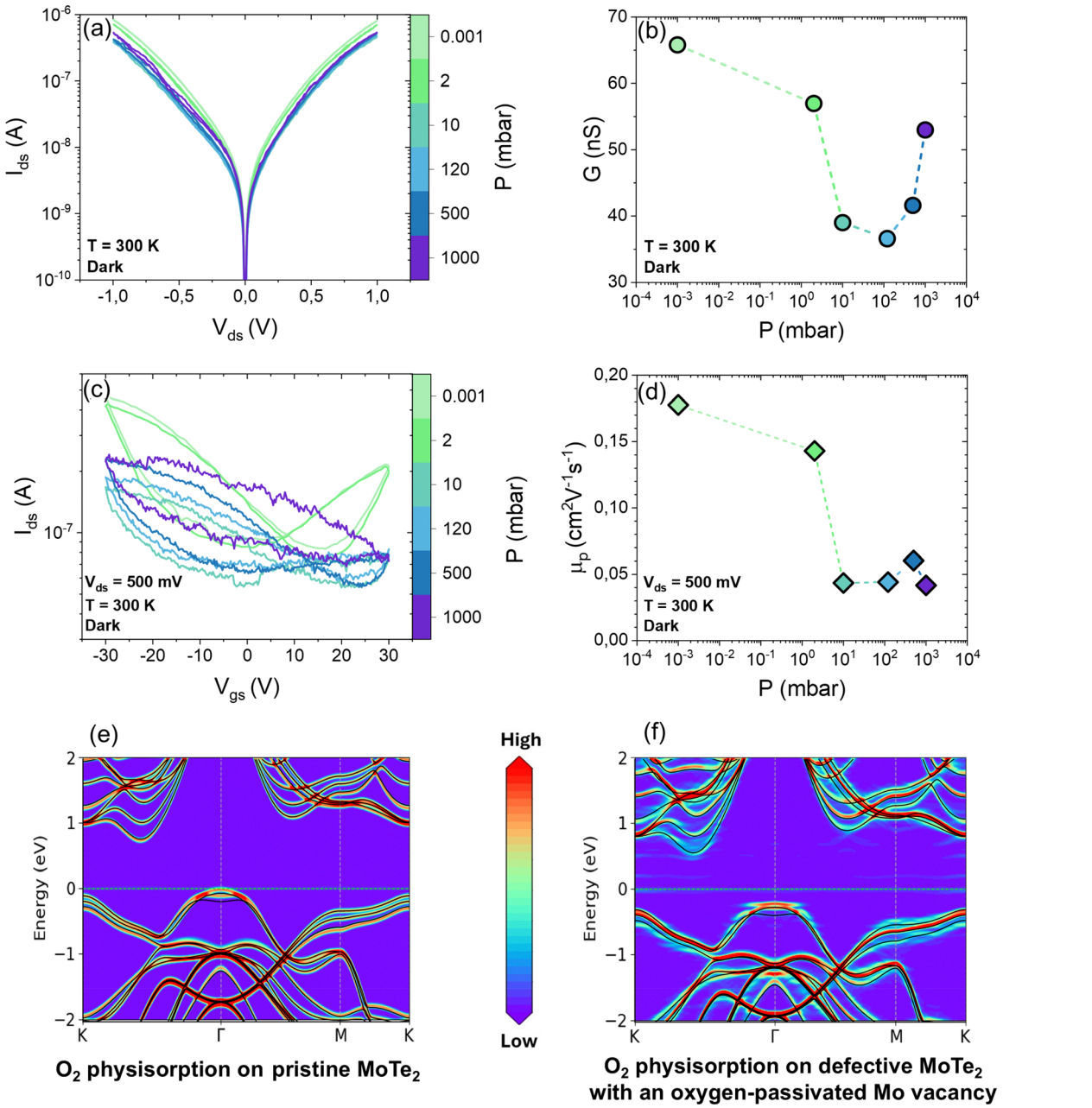

Fig. 6 Electrical characterization as a function of pressure. IV curves at different pressures, increasing from 10^{-3} mbar up to 1 bar (a). Corresponding conductance as a function of pressure (b). Transfer characteristics at V_{ds} = 500 mV for different pressures (c). Pressure dependence of the hole field-effect mobility (d). Unfolded band structure of O_2 physisorption on the surface of pristine $MoTe_2$ (e), and defective $MoTe_2$ with an oxygen-passivated Mo vacancy (f). Black solid lines in (e) and (f) denote the primitive-cell band structure of pristine $MoTe_2$. The zero of energy corresponds to the Fermi level. All measurements in (a)–(d) were conducted in the dark and at room temperature.

extracted from the IV curves at small biases, where the current grows linearly with V_{ds}. The initial reduction in conductivity can be explained by the increasing density of scattering centers with pressure. However, to fully understand this non-monotonic trend one must also consider hole mobility. Fig. 6c reports the transfer curves at the different pressures during the sweep. Starting from a post-annealing configuration, with slight ambipolar behavior, the n-type conduction is gradually suppressed due to electronic trapping in adsorbate-induced defect states. The presence of adsorbates on the channel is reflected in noisier curves at higher pressures. The trend of hole mobility is shown in Fig. 6d. μ_p decreases since it linearly depends on the scattering time τ which decreases as the concentration of adsorbates on the channel becomes higher. At first, the conductance $G \propto \mu_p p$ (p is the hole density) follows the trend of μ_p, suggesting that p is not subject to significant variations. When a pressure of 10^2 mbar is reached, mobility stops decreasing and G starts to increase. From this pressure onwards, the adsorbate related hole concentration possibly becomes dominant, with a consequent p-doping of the channel. The DFT calculations reported in Fig. 6e and f confirm the p-type doping effect of oxygen physisorption on both pristine $MoTe_2$ and defective $MoTe_2$ with an oxygen-passivated Mo vacancy.

4. Conclusions

This study investigates the electrical behavior of $MoTe_2$-based field-effect transistors through a combined experimental and theoretical approach. All measurements were performed in the dark using a two-probe configuration. The device exhibits Schottky barriers at the metal/semiconductor interfaces, while the transfer characteristics consistently show p-type behavior, with enhanced conduction under vacuum conditions. Although the studied devices show limited FET performance, this is not a limitation for the present study, which focuses on clarifying the role of defects and trap states in charge transport. Under high vacuum conditions, an increase in mobility with V_{ds} bias is observed, which may be associated with a reduction in contact resistance, accompanied by a reduction in the I_{ON}/I_{OFF} ratio. Temperature-dependent measurements yield nearly symmetric Schottky barrier heights under positive and negative drain biases, $\Phi_B^{V>0}$ = 38 meV and $\Phi_B^{V<0}$ = 37 meV, respectively. Analysis of the temperature dependence of the mobility suggests that ionized-impurity scattering is an important transport mechanism below 300 K, possibly consistent with the presence of unpassivated Te and Mo vacancies. At higher temperatures, acoustic-phonon scattering appears to become the prevailing mechanism. Both the SS and the V_{th} increase exponentially with temperature, in agreement with thermally activated transport from band-tail states. Following thermal annealing, a reduction in channel conductance under vacuum is observed, suggesting a possible role of oxygen passivation of vacancies leads to a suppression of p-doping. Finally, increasing measurement chamber pressure enhances molecular adsorption, which is consistent with a reduction in both mobility and conductance through introducing additional scattering processes; however, near atmospheric pressure, the p-doping effect of adsorbates appears to become significant. In summary, this joint experimental and DFT study suggests that distinct classes of defects, such as intrinsic vacancies, interface/border traps, and surface adsorbates, collectively may govern charge transport in $MoTe_2$ FETs.

Conflicts of interest

There are no conflicts to declare.

Data availability

The data supporting the findings of this study are available from the corresponding authors upon reasonable request.

Acknowledgements

A. D. B. acknowledges the financial support from the University of Salerno, with grant ORSA254881. This work was also supported by Research Ireland (formerly Science Foundation Ireland) through the AMBER Research Centre (SFI-12/RC/2278_P2) and the Frontiers for the Future PI Award (24/FFP-A/13329). Support from the EU MSCA project 101153933 is also acknowledged. The authors acknowledge the SFI/HEA Irish Centre for High-End Computing (ICHEC) for the provision of computational facilities and support. The authors also acknowledge K. Momma and F. Izumi for the software support.[115]

References

1 W. Ren, P. Boggild, J. M. Redwing, K. S. Novoselov, L. Sun, Y. Qi, K. Jia, Z. Liu, O. Burton, J. A. Alexander-Webber, S. Hofmann, Y. Cao, Y. Long, Q.-H. Yang, D. Li, S. H. Choi, K. K. Kim, Y. H. Lee, M. Li, Q. Huang, Y. Gogotsi, N. Clark, A. Carl, R. Gorbachev, T. Olsen, J. Rosen, K. S. Thygesen, D. K. Efetov, B. S. Jessen, M. Yankowitz, J. Barrier, R. K. Kumar, F. Koppens, H. Deng, X. Li, S. Dai, D. Basov, X. Wang, S. Das, X. Duan, Z. Yu, M. Borsch, A. C. Ferrari, R. Huber, M. Kira, F. Xia, X. Wang, Z.-S. Wu, X. Feng, P. Simon, H.-M. Cheng, B. Liu, Y. Xie, W. Jin, R. R. Nair, Y. Xu, H.-B. Zhang, V. Pellegrini, B. Qu, M. Lemme, A. Katiyar, J.-H. Ahn, I. Aharonovich, M. C. Hersam, S. Roche, Q. Hua, G. Shen, T.-L. Ren, C. M. Koo, N. A. Koratkar, R. J. Young and A. Pollard, *2D Mater.*, 2026, **13**, 021501.
2 A. Di Bartolomeo, *Nanomaterials*, 2020, **10**, 579.
3 M. B. Askari, P. Salarizadeh, P. Veisi, E. Samiei, H. Saeidfirozeh, M. T. Tourchi Moghadam and A. Di Bartolomeo, *Micromachines*, 2023, **14**, 691.
4 V. Patil, J. Kim, K. Agrawal, T. Park, J. Yi, N. Aoki, K. Watanabe, T. Taniguchi and G.-H. Kim, *Nanotechnology*, 2021, **32**, 325603.

5 M. W. Iqbal, M. Z. Iqbal, M. F. Khan, M. A. Shehzad, Y. Seo, J. H. Park, C. Hwang and J. Eom, *Sci. Rep.*, 2015, **5**, 10699.
6 S. Sim, S. Li, W. Cai, B. Yu, X. Ju, J. Cao, Z. Dong, X. Yin, S. Shin, Y. Luo, D. Chi, A. Suwardi, H. K. Ng and J. Wu, *Adv. Sci.*, 2025, **12**, e09170.
7 S. H. Mir, V. K. Yadav and J. K. Singh, *ACS Omega*, 2020, **5**, 14203–14211.
8 O. Durante, K. Intonti, L. Viscardi, S. De Stefano, E. Faella, A. Kumar, A. Pelella, F. Romeo, F. Giubileo, M. S. G. Alghamdi, M. A. S. Alshehri, M. F. Craciun, S. Russo and A. Di Bartolomeo, *ACS Appl. Nano Mater.*, 2023, **6**, 21663–21670.
9 K. Intonti, A. Mazzotti, A. Pelella, F. Giubileo, N. Martucciello, S. O'Sullivan, V. Patil, P. K. Hurley, L. Ansari, F. Gity and A. Di Bartolomeo, *Mater. Horiz.*, 2026, **13**, 2583–2594.
10 T. Knobloch, S. Selberherr and T. Grasser, *Nanomaterials*, 2022, **12**, 3548.
11 Y. Wang, Z. Pan, T. Zhou, X. Li, C. Luo, T. Zheng, W. Gao, Y. Zhang, Y. Yang, J. Li and N. Huo, *Mater. Sci. Eng., R*, 2025, **165**, 101020.
12 Y. Zhang, S. Hu, Y. Zhou, T. Xu, Y. Peng, H. Deng, X. Bao and X. Zeng, *J. Electron. Mater.*, 2023, **52**, 5218–5226.
13 A. Mazzotti, K. Intonti, L. Viscardi, O. Durante, A. Spuri, A. Di Bernardo and A. Di Bartolomeo, *2025 IEEE 25th International Conference on Nanotechnology (NANO)*, IEEE, Washington, DC, USA, 2025, pp. 255–260.
14 T. D. Ngo, Z. Yang, M. Lee, F. Ali, I. Moon, D. G. Kim, T. Taniguchi, K. Watanabe, K. Lee and W. J. Yoo, *Adv. Electron. Mater.*, 2021, **7**, 2001212.
15 C. D. Ornelas, A. Bowman, T. S. Walmsley, T. Wang, K. Andrews, Z. Zhou and Y.-Q. Xu, *ACS Appl. Mater. Interfaces*, 2020, **12**, 46476–46482.
16 J. Ding, X. Wang, Z. Song, S. Wang, Y. Lu, W. Wang, T. Han, F. Li, X. Zhu, L. Shan and M. Long, *Adv. Sens. Res.*, 2023, **2**, 2300029.
17 A. Pelella, A. Kumar, K. Intonti, O. Durante, S. De Stefano, X. Han, Z. Li, Y. Guo, F. Giubileo, L. Camilli, M. Passacantando, A. Zak and A. Di Bartolomeo, *Small*, 2024, **20**, 2403965.
18 J.-K. Ko, I.-H. Park, K. Hong and K. C. Kwon, *Nanomaterials*, 2024, **14**, 1397.
19 A. Mirzaei, M. Alizadeh, H. R. Ansari, M. Moayedi, Z. Kordrostami, H. Safaeian, M. H. Lee, T. Kim, J. Kim, H. W. Kim and S. S. Kim, *Nanotechnology*, 2024, **35**, 332002.
20 A. Kumar, K. Intonti, L. Viscardi, O. Durante, A. Pelella, O. Kharsah, S. Sleziona, F. Giubileo, N. Martucciello, P. Ciambelli, M. Schleberger and A. Di Bartolomeo, *Mater. Horiz.*, 2024, **11**, 2397–2405.
21 M. H. Pervez, E. Elahi, M. A. Khan, M. Nasim, M. Asim, A. Rehmat, M. A. Rehman, M. A. Assiri, S. Rehman, J. Eom and M. F. Khan, *Small Struct.*, 2025, **6**, 2400386.
22 S. De Stefano, O. Durante, A. Sessa, A. Politano, G. D'Olimpio, T. Dadiani, E. Faella, A. Dinescu, C. Parvulescu, C. Hetherington, C.-N. Kuo, C. S. Lue, M. Aldrigo, M. Passacantando and A. Di Bartolomeo, *ACS Appl. Mater. Interfaces*, 2025, **17**, 50901–50915.
23 J. Sung, S. W. Kim, D. Lee, S. Moon, E. Lee and H. H. Kim, *Small*, 2025, **21**, 2504024.
24 L. Viscardi, A. Mazzotti, O. Durante, T. Pucher, N. Martucciello, A. Castellanos-Gomez and A. D. Bartolomeo, *J. Phys. D: Appl. Phys.*, 2025, **58**, 265102.
25 P. Saha, M. Sahad E, S. Sathyanarayana and B. C. Das, *ACS Nano*, 2024, **18**, 1137–1148.
26 N. Krishnan K, S. Sathyanarayana and B. C. Das, *J. Mater. Chem. C*, 2024, **12**, 13827–13839.
27 M. K. Ghimire, H. Ji, H. Z. Gul, H. Yi, J. Jiang and S. C. Lim, *ACS Appl. Mater. Interfaces*, 2019, **11**, 10068–10073.
28 A. Sessa, S. De Stefano, O. Durante, A. Pelella, M. Aldrigo, C. Parvulescu, A. Dinescu, C. Kuo, C. S. Lue, T. Dadiani, G. D'Olimpio, E. Faella, A. Politano, M. Passacantando and A. Di Bartolomeo, *Adv. Electron. Mater.*, 2026, e00734.
29 Q. H. Wang, K. Kalantar-Zadeh, A. Kis, J. N. Coleman and M. S. Strano, *Nat. Nanotechnol.*, 2012, **7**, 699–712.
30 D. P. Gulo, N. T. Hung, R. Sankar, R. Saito and H.-L. Liu, *Phys. Rev. Mater.*, 2023, **7**, 044001.
31 Y. Pan, L. Zhu, L. Lu, J. Ou, J. Zhou, C. An and M. Dong, *Adv. Funct. Mater.*, 2024, **34**, 2407931.
32 J. Wu, D. Luo, P. Wen, X. Han, C. Wang, H. Yu, W. Gao, X. Liu, G. Konstantatos, J. Li and N. Huo, *Adv. Opt. Mater.*, 2022, **10**, 2201902.
33 R. Ma, H. Zhang, Y. Yoo, Z. P. Degregorio, L. Jin, P. Golani, J. Ghasemi Azadani, T. Low, J. E. Johns, L. A. Bendersky, A. V. Davydov and S. J. Koester, *ACS Nano*, 2019, **13**, 8035–8046.
34 X. Hu, F. Zhang, Z. Hu, P. He, L. Tao, Z. Zheng, Y. Zhao, Y. Yang and J. He, *Opt. Mater.*, 2023, **136**, 113467.
35 S. S. Awate, K. Xu, J. Liang, B. Katz, R. Muzzio, V. H. Crespi, J. Katoch and S. K. Fullerton-Shirey, *ACS Nano*, 2023, **17**, 22388–22398.
36 H. Kowalczyk, J. Biscaras, N. Pistawala, L. Harnagea, S. Singh and A. Shukla, *ACS Nano*, 2023, **17**, 6708–6718.
37 Y. Tan, F. Luo, M. Zhu, X. Xu, Y. Ye, B. Li, G. Wang, W. Luo, X. Zheng, N. Wu, Y. Yu, S. Qin and X.-A. Zhang, *Nanoscale*, 2018, **10**, 19964–19971.
38 S. Yang, X. Xu, W. Xu, B. Han, Z. Ding, P. Gu, P. Gao and Y. Ye, *ACS Appl. Nano Mater.*, 2020, **3**, 10411–10417.
39 Y. Jeong, B. Han, A. Tamayo, N. Claes, S. Bals and P. Samorì, *ACS Nano*, 2024, **18**, 18334–18343.
40 K. Intonti, A. Sessa, H. Neill, V. Patil, A. Pelella, N. Martucciello, L. Ansari, P. K. Hurley, F. Gity and A. Di Bartolomeo, *2025 IEEE 25th International Conference on Nanotechnology (NANO)*, IEEE, Washington, DC, USA, 2025, pp. 588–593.
41 Y. Lin, Y. Xu, S. Wang, S. Li, M. Yamamoto, A. Aparecido-Ferreira, W. Li, H. Sun, S. Nakaharai, W. Jian, K. Ueno and K. Tsukagoshi, *Adv. Mater.*, 2014, **26**, 3263–3269.
42 V. Patil, H. Neill, B. Sheehan, P. K. Hurley, L. Ansari and F. Gity, *Adv. Electron. Mater.*, 2025, **11**, e00305.
43 G. Stan, C. V. Ciobanu, S. R. J. Likith, A. Rani, S. Zhang, C. A. Hacker, S. Krylyuk and A. V. Davydov, *ACS Appl. Mater. Interfaces*, 2020, **12**, 18182–18193.
44 O. F. N. Okello, D.-H. Yang, S.-Y. Seo, J. Park, G. Moon, D. Shin, Y.-S. Chu, S. Yang, T. Mizoguchi, M.-H. Jo and S.-Y. Choi, *ACS Nano*, 2024, **18**, 6927–6935.

45 W. Luo, M. Zhu, G. Peng, X. Zheng, F. Miao, S. Bai, X. Zhang and S. Qin, *Adv. Funct. Mater.*, 2018, **28**, 1704539.
46 S. Larentis, B. Fallahazad, H. C. P. Movva, K. Kim, A. Rai, T. Taniguchi, K. Watanabe, S. K. Banerjee and E. Tutuc, *ACS Nano*, 2017, **11**, 4832–4839.
47 B. Yu, W. Kim, J. Jang, J. Lee, J. P. Hong, N. Kwon, S. Kim, A. Ha, H. Kim, J. Ahn, K. Jeong, T. Taniguchi, K. Watanabe, G. Wang, J. Ahn, S. Park and D. K. Hwang, *Adv. Funct. Mater.*, 2024, **34**, 2404129.
48 G. Y. Bae, J. Kim, J. Kim, S. Lee and E. Lee, *Nanomaterials*, 2021, **11**, 2805.
49 Q. Wang, J. Chen, Y. Zhang, L. Hu, R. Liu, C. Cong and Z.-J. Qiu, *Nanomaterials*, 2019, **9**, 756.
50 J.-H. Li, D. Bing, Z.-T. Wu, G.-Q. Wu, J. Bai, R.-X. Du and Z.-Q. Qi, *Chin. Phys. B*, 2020, **29**, 017802.
51 M. Yamamoto, S. T. Wang, M. Ni, Y.-F. Lin, S.-L. Li, S. Aikawa, W.-B. Jian, K. Ueno, K. Wakabayashi and K. Tsukagoshi, *ACS Nano*, 2014, **8**, 3895–3903.
52 X. Luo, Y. Zhao, J. Zhang, M. Toh, C. Kloc, Q. Xiong and S. Y. Quek, *Phys. Rev. B: Condens. Matter Mater. Phys.*, 2013, **88**, 195313.
53 C. Ruppert, B. Aslan and T. F. Heinz, *Nano Lett.*, 2014, **14**, 6231–6236.
54 H. Li, Q. Zhang, C. C. R. Yap, B. K. Tay, T. H. T. Edwin, A. Olivier and D. Baillargeat, *Adv. Funct. Mater.*, 2012, **22**, 1385–1390.
55 W. Zhao, Z. Ghorannevis, K. K. Amara, J. R. Pang, M. Toh, X. Zhang, C. Kloc, P. H. Tan and G. Eda, *Nanoscale*, 2013, **5**, 9677.
56 S. Smidstrup, T. Markussen, P. Vancraeyveld, J. Wellendorff, J. Schneider, T. Gunst, B. Verstichel, D. Stradi, P. A. Khomyakov, U. G. Vej-Hansen, M.-E. Lee, S. T. Chill, F. Rasmussen, G. Penazzi, F. Corsetti, A. Ojanperä, K. Jensen, M. L. N. Palsgaard, U. Martinez, A. Blom, M. Brandbyge and K. Stokbro, *J. Phys.: Condens. Matter*, 2020, **32**, 015901.
57 M. J. Van Setten, M. Giantomassi, E. Bousquet, M. J. Verstraete, D. R. Hamann, X. Gonze and G.-M. Rignanese, *Comput. Phys. Commun.*, 2018, **226**, 39–54.
58 H. J. Monkhorst and J. D. Pack, *Phys. Rev. B: Condens. Matter Mater. Phys.*, 1976, **13**, 5188–5192.
59 S. Grimme, J. Antony, S. Ehrlich and H. Krieg, *J. Chem. Phys.*, 2010, **132**, 154104.
60 J. Heyd, G. E. Scuseria and M. Ernzerhof, *J. Chem. Phys.*, 2003, **118**, 8207–8215.
61 V. Patil, H. Neill, B. Sheehan, P. K. Hurley, L. Ansari and F. Gity, *Adv. Electron. Mater.*, 2025, **11**, e00305.
62 S. Kim, J. H. Kim, D. Kim, G. Hwang, J. Baik, H. Yang and S. Cho, *2D Mater.*, 2017, **4**, 024004.
63 G. Makov and M. C. Payne, *Phys. Rev. B: Condens. Matter Mater. Phys.*, 1995, **51**, 4014–4022.
64 T. Kim, D. Joung and J. Park, *Curr. Appl. Phys.*, 2018, **18**, 843–846.
65 S. M. Sze and K. K. Ng, *Physics of Semiconductor Devices*, Wiley, 1st edn, 2006.
66 W. Li, E. Chen, D. Li, Z. Lu, X. Zheng, X. Wang, X. Wan and K. Chen, *Adv. Mater. Technol.*, 2025, **10**, 70024.
67 A. Grillo and A. Di Bartolomeo, *Adv. Electron. Mater.*, 2021, **7**, 2000979.
68 A. Di Bartolomeo, A. Grillo, F. Urban, L. Iemmo, F. Giubileo, G. Luongo, G. Amato, L. Croin, L. Sun, S. Liang and L. K. Ang, *Adv. Funct. Mater.*, 2018, **28**, 1800657.
69 A. Di Bartolomeo, K. Intonti, L. Peluso, R. Di Marco, G. Vocca, F. Romeo, F. Giubileo, A. Grillo and E. Orhan, *Nano Ex.*, 2025, **6**, 022501.
70 A. Sessa, T. Dadiani, S. De Stefano, O. Durante, A. Pelella, C. Parvulescu, A. Dinescu, M. Aldrigo, C. Kuo, C. S. Lue, G. D'Olimpio, E. Faella, A. Politano, M. Passacantando and A. Di Bartolomeo, *Adv. Electron. Mater.*, 2025, **11**, e00327.
71 S. Bitter, P. Schlupp, H. Von Wenckstern and M. Grundmann, *ACS Appl. Mater. Interfaces*, 2017, **9**, 26574–26581.
72 A. Di Bartolomeo, L. Genovese, F. Giubileo, L. Iemmo, G. Luongo, T. Foller and M. Schleberger, *2D Mater.*, 2017, **5**, 015014.
73 S. Abedin, V. Kurtash, S. Mathew, S. Thiele, H. O. Jacobs and J. Pezoldt, *Materials*, 2024, **17**, 1350.
74 A. K. Rai, A. A. Shah, J. Kumar, S. Chattaraj, A. B. Dar, U. Patbhaje and M. Shrivastava, *ACS Nano*, 2024, **18**, 6215–6228.
75 M. W. Iqbal, E. Elahi, A. Amin, S. Aftab, I. Aslam, G. Hussain and M. A. Shehzad, *Superlattices Microstruct.*, 2020, **147**, 106698.
76 D. Qu, X. Liu, M. Huang, C. Lee, F. Ahmed, H. Kim, R. S. Ruoff, J. Hone and W. J. Yoo, *Adv. Mater.*, 2017, **29**, 1606433.
77 F. Giannazzo, G. Fisichella, A. Piazza, S. Di Franco, G. Greco, S. Agnello and F. Roccaforte, *Beilstein J. Nanotechnol.*, 2017, **8**, 254–263.
78 A. Di Bartolomeo, L. Genovese, F. Giubileo, L. Iemmo, G. Luongo, T. Foller and M. Schleberger, *2D Mater.*, 2017, **5**, 015014.
79 D. J. Late, B. Liu, H. S. S. R. Matte, V. P. Dravid and C. N. R. Rao, *ACS Nano*, 2012, **6**, 5635–5641.
80 F. Ahmed, A. M. Shafi, D. M. A. Mackenzie, M. A. Qureshi, H. A. Fernandez, H. H. Yoon, M. G. Uddin, M. Kuittinen, Z. Sun and H. Lipsanen, *Adv. Mater. Interfaces*, 2021, **8**, 2100950.
81 A. Rani, K. DiCamillo, M. A. H. Khan, M. Paranjape and M. E. Zaghloul, *Sensors*, 2019, **19**, 2551.
82 S. Nisar, M. Shahzadi, Z. M. Shahzad, D. Kim, G. Dastgeer and A. Irfan, *ACS Appl. Electron. Mater.*, 2023, **5**, 5714–5721.
83 S. Fathipour, N. Ma, W. S. Hwang, V. Protasenko, S. Vishwanath, H. G. Xing, H. Xu, D. Jena, J. Appenzeller and A. Seabaugh, *Appl. Phys. Lett.*, 2014, **105**, 192101.
84 M. Zhang, J. Li, K. Shi, X. Fang, Y. Zhai, G. Qu, W. Wang and Z. Jiang, *Mater. Res. Bull.*, 2025, **185**, 113275.
85 Y. Jeong, B. Han, A. Tamayo, N. Claes, S. Bals and P. Samorì, *ACS Nano*, 2024, **18**, 18334–18343.
86 Y. Kim, A. Venkatesan, J. Kim, H. Kim, K. Watanabe, T. Taniguchi, D. Whang and G.-H. Kim, *Mater. Sci. Semicond. Process.*, 2023, **153**, 107133.
87 W. Huang, Y. Zhang, M. Song, B. Wang, H. Hou, X. Hu, X. Chen and T. Zhai, *Chin. Chem. Lett.*, 2022, **33**, 2281–2290.

88 Y. Park, H. W. Baac, J. Heo and G. Yoo, *Appl. Phys. Lett.*, 2016, **108**, 083102.
89 H. Jawa, A. Varghese and S. Lodha, *ACS Appl. Mater. Interfaces*, 2021, **13**, 9186–9194.
90 A. Di Bartolomeo, A. Pelella, X. Liu, F. Miao, M. Passacantando, F. Giubileo, A. Grillo, L. Iemmo, F. Urban and S. Liang, *Adv. Funct. Mater.*, 2019, **29**, 1902483.
91 A. Mazzotti, O. Durante, S. De Stefano, L. Viscardi, A. Pelella, O. Kharsah, L. Daniel, S. Sleziona, M. Schleberger and A. Di Bartolomeo, *Adv. Opt. Mater.*, 2025, **13**, 2500811.
92 R. T. Tung, *Phys. Rev. B: Condens. Matter Mater. Phys.*, 1992, **45**, 13509–13523.
93 A. S. Kavasoglu, C. Tozlu, O. Pakma, N. Kavasoglu, S. Ozden, B. Metin, O. Birgi and S. Oktik, *J. Phys. D: Appl. Phys.*, 2009, **42**, 145111.
94 Ş. Aydoğan, M. Sağlam, A. Türüt and Y. Onganer, *Synth. Met.*, 2005, **150**, 15–20.
95 J. H. Werner and H. H. Güttler, *J. Appl. Phys.*, 1991, **69**, 1522–1533.
96 R. T. Tung, *Mater. Sci. Eng., R*, 2001, **35**, 1–138.
97 J. Tersoff, *Phys. Rev. Lett.*, 1984, **52**, 465–468.
98 J. Bardeen, in *Electronic Structure of Metal–Semiconductor Contacts*, ed. W. Mönch, Springer, Netherlands, Dordrecht, 1999, vol. 4, pp. 63–73.
99 K. K. Chin, R. Cao, T. Kendelewicz, K. Miyano, M. D. Williams, S. Doniach, I. Lindau and W. E. Spicer, *MRS Proc.*, 1986, **77**, 297.
100 X. Liu, M. S. Choi, E. Hwang, W. J. Yoo and J. Sun, *Adv. Mater.*, 2022, **34**, 2108425.
101 C. Kim, I. Moon, D. Lee, M. S. Choi, F. Ahmed, S. Nam, Y. Cho, H.-J. Shin, S. Park and W. J. Yoo, *ACS Nano*, 2017, **11**, 1588–1596.
102 J. Xie, N. M. Patoary, G. Zhou, M. Y. Sayyad, S. Tongay and I. S. Esqueda, *Nanotechnology*, 2022, **33**, 225702.
103 N. Huo, Y. Yang, Y.-N. Wu, X.-G. Zhang, S. T. Pantelides and G. Konstantatos, *Nanoscale*, 2018, **10**, 15071–15077.
104 K. S. Bhargavi and S. S. Kubakaddi, *J. Phys.: Condens. Matter*, 2014, **26**, 485013.
105 A. Pelella, V. Demontis, A. Sessa, A. Mazzotti, F. Giubileo, V. Zannier, L. Sorba, F. Rossella and A. Di Bartolomeo, *Adv. Electron. Mater.*, 2025, **11**, e00520.
106 N. S. Ndiaye, O. Simonetti, T.-P. Nguyen and L. Giraudet, *Org. Electron.*, 2021, **99**, 106350.
107 Y. Shao, J. Yoon, H. Kim, T. Lee and W. Lu, *Appl. Surf. Sci.*, 2014, **301**, 2–8.
108 G. Kim, D. X. Dang, H. Z. Gul, H. Ji, E. K. Kim and S. C. Lim, *Nanotechnology*, 2024, **35**, 035702.
109 H. Ji, G. Lee, M.-K. Joo, Y. Yun, H. Yi, J.-H. Park, D. Suh and S. C. Lim, *Appl. Phys. Lett.*, 2017, **110**, 183501.
110 V. O. Khaustov, J. Köster, M. W. Ochapski, A. A. Zakharov, D. Convertino, Z. M. Gebeyehu, L. Martini, N. Mishra, G. Marini, M. Calandra, U. Kaiser, S. Forti and C. Coletti, *2D Mater.*, 2025, **12**, 025025.
111 H. Ryu, Y. Lee, J. H. Jeong, Y. Lee, Y. Cheon, K. Watanabe, T. Taniguchi, K. Kim, H. Cheong, C. Lee and G. Lee, *Small*, 2023, **19**, 2205224.
112 C. Wang, X. Liu, X. Li, Z. Yao, W. Hong and T. Jiao, *ACS Mater. Lett.*, 2026, **8**, 76–98.
113 B. S. Y. Kim, T. D. Ngo, Y. Hassan, S. H. Chae, S. Yoon and M. S. Choi, *Adv. Sci.*, 2024, **11**, 2407175.
114 B. Sirota, N. Glavin, S. Krylyuk, A. V. Davydov and A. A. Voevodin, *Sci. Rep.*, 2018, **8**, 8668.
115 K. Momma and F. Izumi, VESTA 3 for three-dimensional visualization of crystal, volumetric and morphology data, *J. Appl. Crystallogr.*, 2011, **44**, 1272–1276.